

## Gravitational-wave astrophysics with effective-spin measurements: asymmetries and selection biases

KEN K. Y. NG,<sup>1,2</sup> SALVATORE VITALE,<sup>1,2</sup> AARON ZIMMERMAN,<sup>3</sup> KATERINA CHATZIOANNOU,<sup>3</sup> DAVIDE GEROSA,<sup>4,\*</sup> AND CARL-JOHAN HASTER<sup>3</sup>

<sup>1</sup>*LIGO, Massachusetts Institute of Technology, Cambridge, Massachusetts 02139, USA*

<sup>2</sup>*Department of Physics and Kavli Institute for Astrophysics and Space Research, Massachusetts Institute of Technology, Cambridge, Massachusetts 02139, USA*

<sup>3</sup>*Canadian Institute for Theoretical Astrophysics, 60 St. George Street, University of Toronto, Toronto, ON M5S 3H8, Canada*

<sup>4</sup>*TAPIR 350-17, California Institute of Technology, 1200 E California Boulevard, Pasadena, CA 91125, USA*

(Dated: August 19, 2022)

### ABSTRACT

Gravitational waves emitted by coalescing compact objects carry information about the spin of the individual bodies. However, with present detectors only the mass-weighted combination of the components of the spin along the orbital angular momentum can be measured accurately. This quantity, the effective spin  $\chi_{\text{eff}}$ , is conserved up to at least the second post-Newtonian order. The measured distribution of  $\chi_{\text{eff}}$  values from a population of detected binaries, and in particular whether this distribution is symmetric about zero, encodes valuable information about the underlying compact-binary formation channels. In this paper we focus on two important complications of using the effective spin to study astrophysical population properties: (i) an astrophysical distribution for  $\chi_{\text{eff}}$  values which is symmetric does not necessarily lead to a symmetric distribution for the detected effective spin values, leading to a *selection bias*; and (ii) the posterior distribution of  $\chi_{\text{eff}}$  for individual events is *asymmetric* and it cannot usually be treated as a Gaussian. We find that the posterior distributions for  $\chi_{\text{eff}}$  systematically show fatter tails toward larger positive values, unless the total mass is large or the mass ratio  $m_2/m_1$  is smaller than  $\sim 1/2$ . Finally we show that uncertainties in the measurement of  $\chi_{\text{eff}}$  are systematically larger when the true value is negative than when it is positive. All these factors can bias astrophysical inference about the population when we have more than  $\sim 100$  events and should be taken into account when using gravitational-wave measurements to characterize astrophysical populations.

*Keywords:* Gravitational waves, black holes, compact binaries, LIGO.

### 1. INTRODUCTION

With the first two scientific runs of the advanced LIGO and VIRGO detectors (Aasi et al. 2015; Acernese et al. 2015) now completed, observations of gravitational waves (GWs) emitted by coalescing binary black hole (BBH) and binary neutron stars (BNS) are becoming routine (Abbott et al. 2016c,b, 2017a,b,c,d). Rates inferred for the merger of compact objects imply that dozens of sources will be detected every year by current ground-based detectors at design sensitivity (Abbott et al. 2016a, 2017d, 2016f,e). Such rates will allow us to move beyond

characterizing individual objects to characterizing whole populations, revealing details about the underlying astrophysics of compact binaries.

The spins of the two merging objects are among the cleanest indicators of the underlying formation channels (though other have been proposed, e.g. the orbital eccentricity, see Nishizawa et al. 2016, 2017; Breivik et al. 2016). In fact, the main proposed formation pathways for compact-binary coalescences (CBCs) result in different distributions for the orientations of the component spins (Mandel & O’Shaughnessy 2010). Systems formed via dynamical interactions in globular clusters (Benacquista & Downing 2013) or stellar clusters near active galactic nuclei (Miller & Lauburg 2009) are typically expected to have a random distribution of the spins’ angles.

kenkyng@mit.edu

\* Einstein Fellow

Conversely, binaries formed through common envelope evolution in galactic fields (Postnov & Yungelson 2014) are expected to have spins preferentially aligned with their orbital angular momentum.

The exact degree of alignment and randomness predicted by both channels is still an open question. Recent cluster observations (Corsaro et al. 2017) found that the progenitor cloud’s angular momentum might have a strong impact on the stellar spins, thus imprinting some preferential direction to the spins of the resulting compact objects. For field binaries, assumptions on the supernova natal kicks, mass transfer, and tidal interactions have all been shown to be crucial in predicting the residual misalignments (Kalogera 2000; Belczynski et al. 2008; Gerosa et al. 2013, 2014; Rodriguez et al. 2016; Wysocki et al. 2018a).

The first quantitative studies on inferring the formation channel of binaries using GW observations had the measurement of *individual* spin parameters as their starting point. Vitale et al. (2017c) and Stevenson et al. (2017) showed how if both formation channels (dynamical and in the field) operate, their branching ratio can be measured after  $\sim 100$  events from the measurement of the misalignment angles. However, a combination of the two component spins exists which is measured better than either of them (Ajith et al. 2011; Santamaría et al. 2010; Vitale et al. 2017b). This is the mass-weighted combination of the projection of the two spins along the orbital angular momentum, usually called the *effective spin* parameter,

$$\chi_{\text{eff}} = \frac{\mathbf{S}_1/m_1 + \mathbf{S}_2/m_2}{m_1 + m_2} \cdot \hat{\mathbf{L}}. \quad (1)$$

Furthermore,  $\chi_{\text{eff}}$  is a constant of motion (up to at least the second post-Newtonian order (Blanchet 2014; Racine 2008)) and it is therefore well suited to parametrize the binary evolution (Kesden et al. 2015; Gerosa et al. 2015).

A key signature of the formation channels is whether the intrinsic distribution of  $\chi_{\text{eff}}$  values is symmetric about zero. Since formation in galactic fields is more likely to yield spins roughly aligned with the angular momentum, systems coming from this channel will have a distribution weighted towards positive  $\chi_{\text{eff}}$  (although individual events with  $\chi_{\text{eff}} < 0$  are possible, see Wysocki et al. 2018a). On the other hand, all spin orientations are expected to be equally likely in binaries assembled via dynamical interactions, which results in a distribution for  $\chi_{\text{eff}}$  *symmetric* about zero. Farr et al. (2017, 2018) exploited this idea to show that if all sources come from the same formation channel the required number of BBH detections to identify it can be as small as a few tens. If both channels operate simultaneously, hundreds of events

are required to calculate their branching ratio and characteristic parameters (Talbot & Thrane 2017). Similar reasonings have also been applied to BNS systems, see e.g. Zhu et al. (2017).

In this paper we point out several important caveats that can affect astrophysical inference based solely on the  $\chi_{\text{eff}}$  distribution of detected events. First, the length of the GW signal depends on the sign of  $\chi_{\text{eff}}$ : for the same masses, systems with  $\chi_{\text{eff}} > 0$  take longer to merge and are thus easier to detect than systems with negative  $\chi_{\text{eff}}$ . This implies that, even if the underlying population were to be perfectly symmetric, the  $\chi_{\text{eff}}$  distribution of detected sources will show a bias toward positive values. Second, the individual posterior distributions of  $\chi_{\text{eff}}$  present a different morphology, depending on whether the true value is positive or negative (with other binary parameters fixed). We show that it is easier to exclude negative values in the inferred value of  $\chi_{\text{eff}}$  if the true value of  $\chi_{\text{eff}}$  is positive, than the other way around, unless the two component masses are very different. In addition, the uncertainty in the measurement of  $\chi_{\text{eff}}$  is systematically larger when the true value of  $\chi_{\text{eff}}$  is negative than if it is positive. Finally, we show how these factors can bias astrophysical inference on the underlying populations.

In the appendixes we present an analytical toy model to explain the shape of the  $\chi_{\text{eff}}$  posteriors and a recipe to generate synthetic posteriors and likelihoods. A webpage where users can create their own realistic synthetic posteriors has been setup at [superstring.mit.edu/welcome.html](http://superstring.mit.edu/welcome.html).

## 2. ASYMMETRY IN THE DETECTED $\chi_{\text{eff}}$ DISTRIBUTION

If all CBCs formed via dynamical interaction, one would expect a symmetric distribution for the inferred values of  $\chi_{\text{eff}}$ , centered around zero. However, binaries with spins positively aligned with the orbital angular momentum have to dissipate more angular momentum and therefore take longer to merge (this is known as the orbital hang-up effect, e.g. Damour 2001; Campanelli et al. 2006; Scheel et al. 2015). The waveform is therefore longer for systems with  $\chi_{\text{eff}} > 0$  than for those with  $\chi_{\text{eff}} < 0$ .

Given the the presence of a threshold in the signal-to-noise (SNR) ratio of detectable events, this results in an observational bias in the distribution of  $\chi_{\text{eff}}$  for *detectable* sources. The net result is that even if the true population had  $\chi_{\text{eff}}$  values perfectly symmetric around zero, the *detected* population will show a preference for positive  $\chi_{\text{eff}}$ . If not modeled, this can potentially be mistaken for the presence of a second population

(e.g. galactic field binaries) contributing preferentially to the positive  $\chi_{\text{eff}}$  branch. To quantify the size of this effect, we simulate a perfectly symmetric distribution of sources, and we measure the distribution of  $\chi_{\text{eff}}$  of the sources which survive the SNR cut.

We simulate waveforms corresponding to the inspiral merger and ringdown of BBHs, using the IMRPHENOMPv2 waveform model (Schmidt et al. 2015; Hannam et al. 2014). First, we draw spin directions which are isotropic on the unit sphere, such that our intrinsic population presents a symmetric  $\chi_{\text{eff}}$  distribution peaked at zero. Next, we need to generate values for the magnitude of the individual spins. The impact of the orbital hang-up will critically depend on the dimensionless magnitude of the individual spins  $\chi_i = |\mathbf{S}_i|/m_i \in [0, 1]$ . We therefore consider five different distributions of spin-magnitude  $\chi$ : (i) *uniform in  $\chi$* :  $p(\chi) = 1$ ; (ii) *linear-low*:  $p(\chi) \propto 1 - \chi$ ; (iii) *linear-high*:  $p(\chi) \propto \chi$ ; (iv) *Gaussian-low*:  $p(\chi) = \mathcal{N}(0, 0.05)$ ; (v) *Gaussian-high*:  $p(\chi) = \mathcal{N}(0, 0.25)$ . These choices facilitate comparisons with Farr et al. (2018, 2017) and Vitale et al. (2017a). We also include *uniform-aligned* distribution, which has uniform spin magnitude ( $p(|\boldsymbol{\chi} \cdot \hat{\mathbf{L}}|) = 1/2$ ) parallel to the orbital angular momentum ( $\boldsymbol{\chi} \times \hat{\mathbf{L}} = 0$ ). The component masses  $m_1, m_2$  are drawn from a power law distribution as parametrized in Abbott et al. (2017a), whereas the sky position and distance are sampled uniformly in comoving volume, with the binary randomly oriented.

The SNR for each signal is calculated using different noise spectral densities, representative of the expected performance improvement of the LIGO/Virgo network over the next few years: O2 (2016-17), O3 (2018-19) and Design (2020) (Abbott et al. 2016d). For O2 and O3 we use the top and bottom of the band labeled “2016-17” in Abbott et al. 2016d. Events are then filtered using a single-interferometer SNR threshold of 8 (Abadie et al. 2010), but we have verified results look qualitatively similar, with a slightly smaller bias, if a more relaxed threshold of 5 is used.

Figure 1 shows the underlying (blue dashed)  $\chi_{\text{eff}}$  distribution as well as the  $\chi_{\text{eff}}$  distribution of detectable binaries (green solid) using the O2 sensitivity curve for the uniform-aligned spin distribution. From Eq. (1),  $\chi_{\text{eff}}$  is defined between -1 (both spins are maximal and anti-aligned with the angular momentum) and +1 (both spins are maximal and co-aligned with the angular momentum). Negligible values of  $\chi_{\text{eff}}$  can be due to either small spin magnitudes or spins vectors perpendicular to the angular momentum. The distribution of  $\chi_{\text{eff}}$  for detectable events is clearly biased toward positive values: 62% of detectable sources have  $\chi_{\text{eff}} > 0$ , compared to 50% of the underlying population. If this selection bias were not

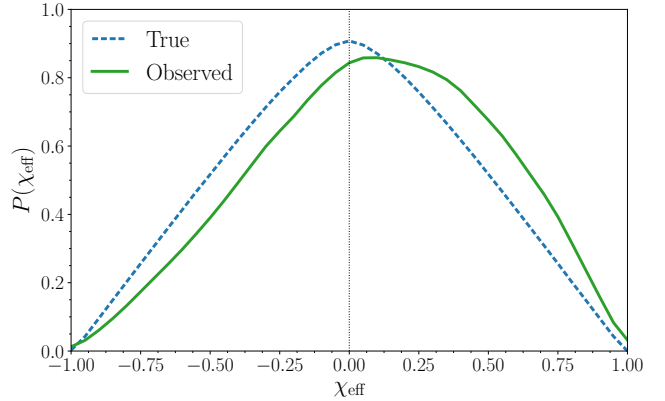


**Figure 1.** The true (blue dashed) and observed (green solid) distribution of  $\chi_{\text{eff}}$  using the O2 sensitivity curve when the true spin magnitudes are uniform-aligned. While true distribution is symmetric around zero, the detectable distribution shows a bias toward positive values.

taken into account, the asymmetry of the green curve in Fig. 1 could be mistaken as arising from a population of systems with preferentially aligned spins.

The uniform-aligned population shown in Fig. 1, however, corresponds to the worst case scenario, as it has the highest probability for large values of  $\chi_{\text{eff}}$ . While for this distribution  $p(|\boldsymbol{\chi} \cdot \hat{\mathbf{L}}|)$  is constant, for all other distributions  $p(|\boldsymbol{\chi} \cdot \hat{\mathbf{L}}|)$  decreases with  $|\boldsymbol{\chi} \cdot \hat{\mathbf{L}}|$ . This results in a smaller probability for  $\chi_{\text{eff}}$  to be large (in magnitude) and consequently smaller biases (Table 1). As expected, the bias becomes negligibly small if the population has preferentially small spin magnitudes (*linear-low*). In the uniform-in- $\chi$  case, the effect is small enough that, even if unaccounted for, it will probably not play a role until  $\mathcal{O}(100)$  of BBHs are detected (which would reduce the statistical uncertainties to a few percent level, comparable with the bias we find) It is worth noting that the uniform-in- $\chi$  distribution has been used as a prior in most GW data analysis to date (cf. Vitale et al. 2017a). For distributions with larger biases, such as the uniform-aligned one illustrated here, not only is the offset from symmetry larger, but also *fewer* sources are required to obtain that level of statistical uncertainty (larger component spins are easier to measure, see e.g. Vitale et al. 2017b).

### 3. ASYMMETRIES IN THE INDIVIDUAL POSTERiors

The measurement of  $\chi_{\text{eff}}$  for many, potentially hundreds, of sources is required to draw conclusions about the underlying astrophysical population. It is therefore natural to first focus on what spin inferences can be made about individual systems, and in particular how often one of the two signs of  $\chi_{\text{eff}}$  can be excluded (cf. Vitale

	O2	O3	Design
Uniform-aligned	12%	11%	11%
Uniform in $\chi$	6%	6%	6%
Linear-high	9%	8%	7%
Linear-low	4%	4%	4%
Gaussian-high	3%	3%	2%
Gaussian-low	0.3%	0.3%	0.3%

**Table 1.** The percent excess of  $\chi_{\text{eff}} > 0$  in the distribution of detectable binaries under various spin distributions and noise levels. 0% means that the distribution is symmetric while, e.g., +12% means that 62% of sources have positive  $\chi_{\text{eff}}$ .

et al. 2017b for a previous partial investigation). Thus far, a significant measurement of the sign of  $\chi_{\text{eff}}$  has been possible only for GW151226, which has  $\chi_{\text{eff}} > 0$  (Abbott et al. 2016b) independent of the prior (Vitale et al. 2017a). For GW170608, most of the posterior for  $\chi_{\text{eff}}$  is positive, but  $\chi_{\text{eff}} = 0$  is found within the 90% credible interval (Abbott et al. 2017b). Posteriors for all the other events do not show a strong preference for either positive or negative values of  $\chi_{\text{eff}}$ . We argue here that parameter correlations need to be addressed carefully before strong conclusions on the underlying astrophysical population can be made.

We start by addressing the following question: if we detected a system like GW151226, but with *negative*  $\chi_{\text{eff}}$ , would we be able to exclude positive values with high confidence? To answer this question, we have created 20 simulated signals with masses and spins compatible with the estimates quoted by Abbott et al. (2016b) for GW151226, rescaling the distances to achieve SNR of either  $\sim 12.5$  (similar to the SNR of GW151226) or  $\sim 33$  (a representative SNR for a loud source). For each source we then create its *flipped* version with the same parameters but  $\mathbf{S}_i \rightarrow -\mathbf{S}_i$  (thus  $\chi_{\text{eff}} \rightarrow -\chi_{\text{eff}}$ ) and a rescaled distance such that the SNR is unchanged. The last step is critical as the orbital hang-up effect would cause the system with negative  $\chi_{\text{eff}}$  to have a lower SNR, thus biasing the comparison. Statistical inference is then performed using the LALINFERENCE pipeline (Veitch et al. 2015) and the reduced order quadrature (ROQ) approximation to the likelihood (Smith et al. 2016). The analyses are done with a zero-noise realization, which ensures the results are representative of the underlying physics, and not due to noise fluctuations (Vallisneri 2008; Rodriguez et al. 2014).

Our results indicate that when the true  $\chi_{\text{eff}}$  is positive it is nearly always possible to exclude negative values. However, the opposite is not true: if the true  $\chi_{\text{eff}}$  is negative, it is rarely the case that the posterior excludes pos-

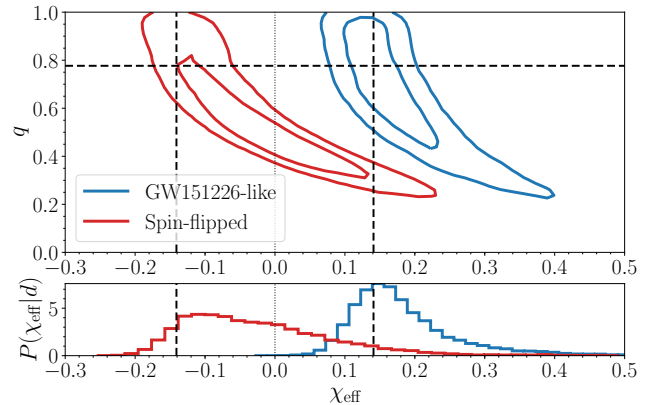


**Figure 2.** The joint  $q$ - $\chi_{\text{eff}}$  posterior distribution for a GW151226-like BBH with positive (blue) or negative (red)  $\chi_{\text{eff}}$ . While the two events differ on the sign of  $\chi_{\text{eff}}$ , all other parameters, including the SNR, are the same. The SNR for this event is  $\sim 12.3$ . The dashed lines indicate the true values of  $\chi_{\text{eff}}$  and mass ratio.

itive values. This is illustrated in Fig. 2, where we show the joint and the marginalized posterior distributions for  $\chi_{\text{eff}}$  and the binary mass ratio  $q = m_2/m_1 \in [0, 1]$  for two of our simulated sources. The island on the right is the joint posterior distribution for a GW151226-like source ( $\chi_{\text{eff}} \sim 0.14$ ), while the one on the left corresponds to the same source with flipped spins ( $\chi_{\text{eff}} \sim -0.14$ ). For both positive and negative  $\chi_{\text{eff}}$ , the marginalized posterior distributions show a clear asymmetry around their median, with a longer tail toward larger (and positive)  $\chi_{\text{eff}}$ , and a much sharper tail on the negative side. The immediate consequence of this asymmetry is that, for this mass ratio, when the true value of  $\chi_{\text{eff}}$  is positive, the posterior distribution is more likely to exclude negative values than it is to exclude positive values when the true  $\chi_{\text{eff}}$  is negative.

The longer tails toward positive values of  $\chi_{\text{eff}}$  can be understood in terms of the well known  $q$ - $\chi_{\text{eff}}$  inspiral degeneracy (Cutler & Flanagan 1994; Poisson & Will 1995; Baird et al. 2013; Pürrer et al. 2013; Chatziioannou et al. 2014, 2015). As shown in Fig. 2 below (see also, e.g., Fig. 4 in Abbott et al. 2016a), joint posterior distributions of these two parameters tend to show a pronounced degeneracy, with low (large) values of  $q$  paired to large (low) values of  $\chi_{\text{eff}}$ . These tails are present in all our GW151226-like simulations, regardless of the sign of  $\chi_{\text{eff}}$ . However, as is already visible Fig. 2, tails tend to be more pronounced when the injected  $\chi_{\text{eff}}$  is negative. Ultimately, this results in higher measurement uncertainties for negative  $\chi_{\text{eff}}$  sources than positive ones. For our GW151226-like simulations, the 90% credible interval for negative  $\chi_{\text{eff}}$  is typically  $\sim 1.5$  larger than

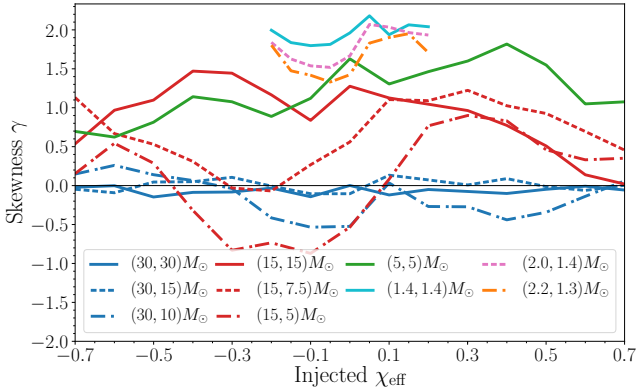


**Figure 3.** The skewness coefficient for the  $\chi_{\text{eff}}$  posterior distributions of all simulated runs. Component masses are given in the legend. For most runs, the skewness is positive, indicating a large tail toward larger  $\chi_{\text{eff}}$ .

for positive ones. We discuss a simple model for these features further in Appendix A.

It is worth stressing that this degeneracy is only present in the inspiral part of the signal. It is therefore expected to be milder for heavier BBHs, which present fewer inspiral cycles in band, and more prominent for lighter BBHs, such as GW151226, and BNSs. In order to verify this, and to check the generality of these trends, we generate another set of simulated signals covering a broader range of system parameters. We consider BBHs with spins  $0 \leq |\chi_{\text{eff}}| \leq 0.7$  (in steps of 0.1 in  $\chi_{\text{eff}}$ ) and seven different values of detector-frame component masses,  $(m_1, m_2) = (30-30), (30-15), (30-10), (15-15), (15-7.5), (15-5), (5-5) M_{\odot}$ . We also simulate BNSs with  $(m_1, m_2) = (2.2-1.3), (2.0-1.4), (1.4-1.4) M_{\odot}$  and effective spins  $0 \leq |\chi_{\text{eff}}| \leq 0.2$  (in steps of 0.05). We generate the BNS signals with the same waveform family used for BBHs (Schmidt et al. 2015; Hannam et al. 2014) and do not include tidal terms. For both BNSs and BBHs, we considered two values of spin tilts ( $10^\circ$  and  $30^\circ$ ), which are defined as the angle between the spins and the angular momentum vector at a GW frequency of 20 Hz, and two values of the network SNR (15 and 30).

Figure 3 shows the skewness coefficient  $\gamma$  (defined here as the third standardized moment of a probability distribution) of the marginalized  $\chi_{\text{eff}}$  posterior for injections with different masses at a fixed SNR of 30 and spin tilt angle of  $10^\circ$  (other runs present very similar results, c.f. D). Values of  $\gamma > 0$  indicate a posterior distribution with a larger tail towards positive values. The skewness is positive for all  $q = 1$  and  $q = 1/2$  BBHs, and for all BNSs.

The skewness approaches zero for heavy BBHs, which is expected since the merger and ringdown phase breaks the  $q$ - $\chi_{\text{eff}}$  degeneracy. Conversely, the skewness increases

for BNS injections, reaching  $\gamma \sim 2$ . For comparison, the skewness for the two posteriors in Fig. 2 are  $\gamma = 1.0$  (1.4) for positive (negative)  $\chi_{\text{eff}}$ .

A few of our simulated sources with  $q = 1/3$  present negative values of  $\gamma$ . These are cases where  $\chi_{\text{eff}}$  and  $q$  are generally *not* measured well, with either a posterior peak not centered at the true value or a very broad posterior distribution (or both), see Appendix D. For these systems with small  $q$ , the best measured parameter is a different combination of masses and spins, namely the 1.5 Post-Newtonian (PN) phase coefficient (Wiseman 1992; Kidder et al. 1993; Cutler & Flanagan 1994; Poisson & Will 1995). We verified that for all sources with negative skewness the 1.5PN coefficient is measured accurately, although  $\chi_{\text{eff}}$  is not. Furthermore, we have verified that in our recovered posteriors this phase term is approximately uncorrelated with the mass ratio.

In Appendix A we present a simple toy model that shows how Gaussian and uncorrelated likelihoods for the mass ratio and the 1.5PN phase term can result in a skewed likelihood and posterior for  $\chi_{\text{eff}}$ . By generating Gaussian likelihood distributions for the symmetric mass ratio and the 1.5PN phase term, performing the appropriate change of coordinates, and taking into account prior bounds, we find that the  $q$ - $\chi_{\text{eff}}$  likelihood profiles have shapes similar to what is obtained from the actual posterior samples and shown in Fig. 2.

Returning to our discussion of the injected and recovered signals, we find that irrespectively of the sign of  $\gamma$ , negative  $\chi_{\text{eff}}$  values are harder to constrain than positive ones. Figure 4 shows the ratios of the 90% credible intervals for  $\chi_{\text{eff}}$  of our systems and of their spin-flipped versions. As expected, we find that this ratio depends on the total mass, and it is smaller the heavier a system is. For 30-30  $M_{\odot}$  BBHs the ratio reaches at most  $\sim 2$ . Lighter systems present much larger ratios. Sources of 15-7.5  $M_{\odot}$ , similar to GW151226, can have an uncertainty for negative  $\chi_{\text{eff}} = -0.4$  up to 4 times larger than for  $\chi_{\text{eff}} = +0.4$ . This factor reaches  $\sim 8$  for  $|\chi_{\text{eff}}| \sim 0.7$ . The  $\chi_{\text{eff}} \sim 0.1$  case is similar to the GW151226-like simulations presented above, where the uncertainty in the measurement of negative  $\chi_{\text{eff}}$  is typically 1.5 times larger than that of the same event with positive  $\chi_{\text{eff}}$ . BNS sources follow a similar trend, with ratios of  $\sim 2$  at  $\chi_{\text{eff}} = |0.2|$ . Already at  $|\chi_{\text{eff}}| = 0.05$ , uncertainties for negative  $\chi_{\text{eff}}$  can be a few tens of percent larger than for positive ones. The ratio of standard deviation looks numerically similar.

We conclude this section with a discussion on the accuracy of the individual  $\chi_{\text{eff}}$  posteriors and the role of priors. As shown by Vitale et al. (2017a) the measurement of  $\chi_{\text{eff}}$  can be significantly impacted by the priors

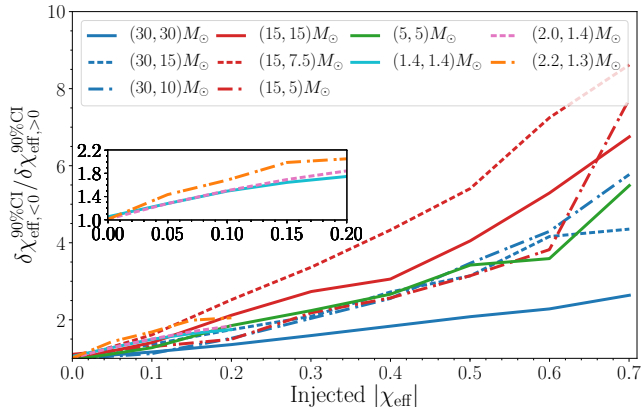


**Figure 4.** Ratio between the 90% credible intervals for sources with negative over positive  $\chi_{\text{eff}}$ . The  $x$ -axis gives the absolute value of the simulated  $\chi_{\text{eff}}$ . Component masses are given in the legend.

one is using in the Bayesian analysis. In the analyses presented in this section, we have used the same priors used by the LIGO-Virgo collaboration for all the events detected up to the second science run (Vitale et al. 2017a refers to this priors as P1). For each compact object, the prior of the spin direction is random on the unit sphere, while the prior of the spin magnitude is uniform in the range  $[0, 0.89]$ , and is discussed further in Appendix A. This results in a prior for  $\chi_{\text{eff}}$  which is peaked at zero (cf. Abbott et al. 2017a, Fig. 5).

We find that this choice leaves a clear imprint in the posterior distribution of the individual events, pushing their medians toward the region of higher prior, i.e. toward zero. This is shown in Fig. 5, where in the  $y$ -axis we report the difference between the median  $\chi_{\text{eff}}$  posterior and the true value, divided by the 90% uncertainty for the systems with SNR 30 and BBH tilt of  $10^\circ$ . For all the events, the shift is indeed in the direction of  $\chi_{\text{eff}}$  closer to zero, and usually smaller than half of the 90% credible interval. The three curves for the BNS sources have been shifted vertically as described in Appendix C. For the runs with SNR 15, the shifts are larger, consistent with the intuition that the prior should matter more for weaker signals. These findings are in agreement with the results of Chatziioannou et al. (2018) on the difficulty of measuring large spins from GW data.

#### 4. IMPACT ON ASTROPHYSICAL INFERENCE

All the effects we have described thus far can, in principle, affect how precisely and accurately one can study the spin distribution of the detected GW sources, and infer their formation channels. In Sec. 2 we saw how the population of the detectable BBH sources will have higher  $\chi_{\text{eff}}$  than that of the true underlying population. In Sec. 3 we have shown that negative  $\chi_{\text{eff}}$  are harder to

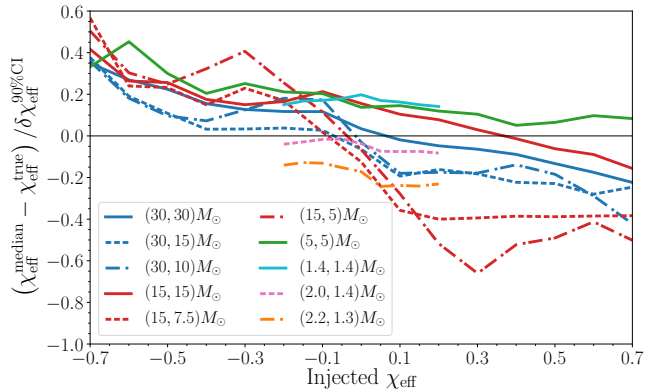


**Figure 5.** The offset in the median of the  $\chi_{\text{eff}}$  posterior for the simulated events with SNR of 30 and tilt (for the BHs only) of  $10^\circ$ , normalized by the width of the 90% credible interval. See Appendix D for medians of more choices of SNR and spins.

measure, and that the posterior distributions for  $\chi_{\text{eff}}$  are often skewed and affected by the priors.

It is natural to ask which of these factors can significantly affect astrophysical inference. For example, the effects of priors should not matter when one does hierarchical modeling, since in that case the likelihood is used, that is: one divides the posterior by the prior used in the analysis. On the other hand, the correlation between mass ratio and  $\chi_{\text{eff}}$  can impact inference solely based on  $\chi_{\text{eff}}$ .

As an example, we repeat one of the analyses performed by Farr et al. (2017). In particular, we assume that two formation channels are possible, one which results in an isotropic distribution of spins, and the other which gives roughly aligned spins. We assume that all black hole sources come from a channel that results in uniform spin magnitudes and isotropic orientations (this is the model “flat-isotropic” or FI in Farr et al. 2017). We focus on  $5-5 M_\odot$  BBH sources, and assume that all of them have SNR of 15. We create a catalog of synthetic BBH sources, having true  $\chi_{\text{eff}}$  drawn from the isotropic distribution (for simplicity, we neglect at first the selection bias described in Sec. 2 - its effect will be described later), and for each of them we create a synthetic posterior distribution. Our goal is to calculate the odds ratio between the isotropic spin and the aligned-spin models (this is the model “flat-aligned” or FA in Farr et al. 2017):  $\mathcal{O}_{\text{iso}}^{\text{align}}$ .

First, we perform an (unrealistic) analysis where each  $\chi_{\text{eff}}$  posterior is a perfect Gaussian centered at the true value with a width of 0.1. Each posterior is divided by its  $\chi_{\text{eff}}$  prior to obtain likelihood distributions suitable for a hierarchical analysis. Using this approach we obtain the curve labeled “Unrealistic” in Fig. 6. Then, we repeat the same analysis by generating synthetic posterior

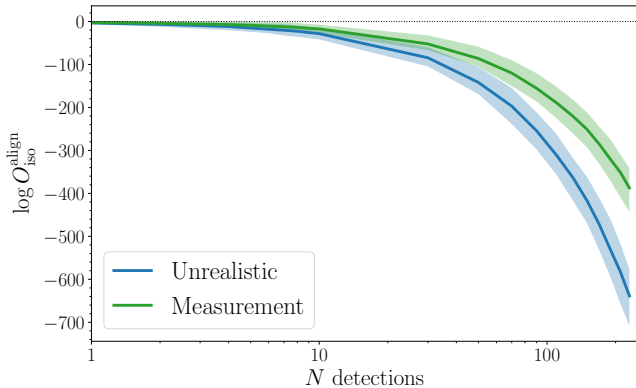


**Figure 6.** Odds ratio between a model where all events have aligned spins vs one where spins are isotropic. The true population has isotropic spins. This is for  $5-5M_{\odot}$ , SNR 15. The unrealistic curve assumes that all  $\chi_{\text{eff}}$  posteriors are centered at the true value.

distributions for all sources using the recipe we provide in Appendix B, which results in skewed posteriors. Critically, we do *not* assume that the posteriors are centered at the true values, but rather we use the results from the previous section to inform the typical offset. Here too we divide each posterior by its prior. These results are labeled “Measurement” in Fig. 6.

Figure 6 shows how the cumulative natural log of  $\mathcal{O}_{\text{iso}}^{\text{ali}}$  evolves as a function of the number of detected sources. The error band reports the spread on the measurement obtained by creating 100 random realizations of the catalog.

We see that the odds ratio for the generalized model are less negative (i.e. favor the isotropic model less) than what is obtained with the unrealistic Gaussian model centered at the true values. This is consistent with the fact that for light equal-mass systems posteriors and likelihood are typically biased toward higher  $\chi_{\text{eff}}$ , Tables 20, 21, 22, 23. After less than one hundred events, the results obtained with a realistic approach vs one in which the true positions of  $\chi_{\text{eff}}$  are known start being clearly different.

The fact that in this case the generalized model does “worse” (gives odds which favor the right model less strongly) is just a consequence of having simulated a population with only perfectly isotropic spins. In a more general situation, both approaches would give biased answers, for different reasons.

To see this we create catalogs where both aligned and isotropic spins are present. Specifically, a fraction  $f_a$  of events will have aligned spins drawn from the flat-aligned distribution, while a fraction  $(1 - f_a)$  will have random spins, coming from the flat-isotropic distribution. First, we perform inference using the realistic posteriors

informed by our MCMC runs, this is the curve labeled as “Measurement” in Fig. 7, where we show the posterior distribution for  $f_a$  as a function of the number of detected events, when the true underlying value of  $f_a$  is 0.5. For each value of  $N$ , we create 100 random catalogs of  $N$  BBHs and calculate the posterior distribution of  $f_a$ . Here, too, we focus on  $5 - 5 M_{\odot}$  BBH sources, and assume that all of them have SNR of 15. The colored band in Fig. 7 are the 90% credible intervals averaged over the 200 catalogs. We see how a clear bias is present: after roughly 180 events, the true value of  $f_a$  is excluded with high confidence. Ultimately, the measurement converges to a value of  $f_a \sim 0.58$ . To verify that the algorithm works as expected, we also consider the (unrealistic) case where each posterior distribution is a Gaussian centered at the true value, with a width informed by our MCMC simulations. This is labeled “Unrealistic” in Fig. 7, and we see how in this idealized scenario the posterior for  $f_a$  converges to the true value.

We have verified that the main contributor to the bias in the “Measurement” curve is not the skewness of the individual posteriors, but rather the fact that for  $5-5 M_{\odot}$  BBHs, the median of the  $\chi_{\text{eff}}$  posterior is systematically offset to the right in our simulations. In deriving the results we have not considered the selection bias discussed in Sec. 2. If included in the analysis, that would further move up the green curve in Fig. 7 by roughly  $\sim 5\%$ , increasing the overall bias. Both types of bias depend quite strongly on the actual properties of the underlying distribution, including mass and mass ratio. For example, if most of the detected BBHs were heavy and roughly equal mass, more detections would be required for the bias to be significant. Our analysis suggests that while tests based on a single parameter,  $\chi_{\text{eff}}$  in this case, might yield reasonable results when only a few tens of sources are detected, in the long term more sophisticated methods will be required. To properly account for correlations and selection effects, higher-dimension hierarchical models should be considered, where all relevant parameters and hyper-parameters are measured at once. This, in turn, might increase the number of sources required to achieve a given level of precision.

## 5. CONCLUSIONS

Measurements of the effective spin  $\chi_{\text{eff}}$  with GW observations can shed light on the formation pathways of black hole and neutron star binaries. In particular, a population with a  $\chi_{\text{eff}}$  distribution symmetric about zero is generally believed to be a solid signature of dynamical formation channels.

In this paper we have shown that such astrophysical statements must be made with care. Even if the underlying

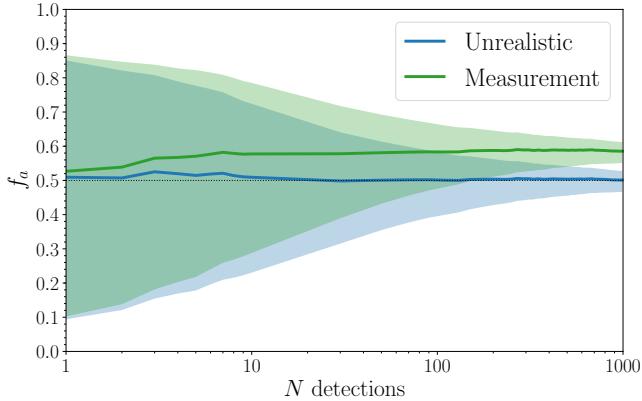


**Figure 7.** The posterior on the fraction of aligned-spin sources,  $f_a$ , as a function of the number of detected events. This is for 5-5 $M_{\odot}$ , SNR 15. The unrealistic curve assumes that all  $\chi_{\text{eff}}$  posteriors are centered at the true value.

ing population were perfectly symmetric in  $\chi_{\text{eff}}$ , several kinds of asymmetries and selection biases affect the final measured distribution.

Because of the orbital hang-up effect, systems with positive  $\chi_{\text{eff}}$  have longer inspirals and hence higher SNRs. They will therefore be detected more easily than sources with negative  $\chi_{\text{eff}}$ . Significant asymmetries also exist in the analysis of *each* event. Due to correlations between the mass ratio and the effective spin, the posterior distribution of  $\chi_{\text{eff}}$  will typically present a prominent tail toward larger (and more positive)  $\chi_{\text{eff}}$ , while no significant tail is present toward more negative values. Furthermore, these tails are generally fatter for sources with negative true  $\chi_{\text{eff}}$ .

This observation carries two key consequences: (i) excluding negative  $\chi_{\text{eff}}$  when the true value is positive is more likely than excluding positive values when the true  $\chi_{\text{eff}}$  is negative, and (ii) if the true  $\chi_{\text{eff}}$  is negative, measurements of it come with larger uncertainties, at fixed SNR.

In other words, measuring positive  $\chi_{\text{eff}}$  is easier, as tentatively confirmed by the GW detections reported to date. For light BBHs like GW151226, we find that an injected negative  $\chi_{\text{eff}}$  yields 90% credible intervals 150% larger than an identical system with a positive  $\chi_{\text{eff}}$  of the same magnitude and same SNR. These effects are milder for heavier BBH, as they accumulate significant signal-to-noise from the merger and ringdown phases,

#### A. MODEL FOR SKEWED POSTERiors

In this section, we present a simple model which recovers the skewed posterior probabilities for  $\chi_{\text{eff}}$ . We

which helps break the degeneracy between  $\chi_{\text{eff}}$  and mass ratio. Conversely, BNSs suffer even more from these observational effects.

It is worth noting that most of the existing studies in the literature that use  $\chi_{\text{eff}}$  to infer properties of the underlying population have generated synthetic Gaussian posterior distributions for  $\chi_{\text{eff}}$ , centered at the true values, with uncertainties informed by the LIGO’s detections (Farr et al. 2018, 2017; Zhu et al. 2017). These studies do not differentiate in any way the correlations present in sources with opposite signs of  $\chi_{\text{eff}}$  and thus do not capture the different morphologies that we have documented in this work.

We have provided a simple recipe to produce synthetic  $\chi_{\text{eff}}$  distributions that are more representative of what is encountered in the actual analysis of gravitational-wave data and used them to verify how the effects described in this paper affect astrophysical inference. We have shown that when using more realistic posterior distributions for  $\chi_{\text{eff}}$ , one is not guaranteed that the astrophysical inference will not be biased. However, this will not be a problem until a few hundreds of detections are made. Once hundreds of events are available, one should use a more elaborate inference scheme, in which all relevant parameters are measured at once (work is ongoing to perform multi-dimensional hierarchical inference, for example to infer the merger rate of BBHs, cf. Wysocki et al. 2018b). Multi-dimensional inference is bound to increase the overall uncertainty, implying that uncovering the formation pathways of compact binary is likely to require more events than claimed in existing work.

*Acknowledgments.* K.N. and S.V. acknowledge support of the MIT physics department through the Solomon Buchsbaum Research Fund, the National Science Foundation, and the LIGO Laboratory. LIGO was constructed by the California Institute of Technology and Massachusetts Institute of Technology with funding from the National Science Foundation and operates under cooperative agreement PHY-0757058. D.G. is supported by NASA through Einstein Postdoctoral Fellowship Grant No. PF6-170152 by the Chandra X-ray Center, operated by the Smithsonian Astrophysical Observatory for NASA under Contract NAS8-03060. The authors acknowledge the LIGO Data Grid clusters. LIGO Document Number P18XYZ

## APPENDIX

consider a PN approximation to the frequency domain waveform, truncating at the 1.5PN term where the first spin contributions appear (Kidder et al. 1993; Blanchet

2014) The 1.5 PN contribution to the phase depends on four parameters, the chirp mass  $\mathcal{M}$ , the symmetric mass ratio  $\eta = q/(1+q)^2$ , and the components of each of the two spin vectors aligned with the orbital angular momentum,  $\chi_{z,i}$ . We can alternatively parametrize the spin dependence by a different pair of independent spin variables, for example  $\chi_{\text{eff}}$  and  $\chi_a = (\chi_{z,1} - \chi_{z,2})/2$ . Using the stationary phase approximation, the 1.5PN phase term can be written as (Cutler & Flanagan 1994)

$$\psi_{1.5} = (\pi \mathcal{M} f)^{-2/3} \psi, \quad (\text{A1})$$

where

$$\psi = \eta^{-3/5} \left[ \frac{(113 - 76\eta)\chi_{\text{eff}} + 76\delta\eta\chi_a}{128} - \frac{3\pi}{8} \right], \quad (\text{A2})$$

$$\delta = \frac{m_1 - m_2}{m_1 + m_2}. \quad (\text{A3})$$

The coefficient of this phase term is measured accurately from the GW signal, and we have verified that in our simulated and recovered signals it is approximately uncorrelated with the mass ratio. It is the coordinate transformation from  $\psi$  to  $\chi_{\text{eff}}$ , along with the physical requirement that  $\eta \leq 0.25$ , that allows to explain the shape of the 2D  $q - \chi_{\text{eff}}$  posteriors and the skewness of the marginalized  $\chi_{\text{eff}}$  posteriors.

To see this, we consider uncorrelated a Gaussian likelihood in  $\eta$  and  $\psi$  for measured GW strain data  $d$ . In this model, we fix  $\mathcal{M}$  to a fiducial value in order to represent the fact that  $\mathcal{M}$  is well measured. As a further simplification, we neglect the spin on the less massive body, setting  $\chi_{z,2} = 0$ , so that  $\chi_{\text{eff}} = \chi_{1,z}/(1+q)$  and  $\chi_a = \chi_{1,z}/2$ . This results in a two-dimensional model, and the likelihood factorizes as

$$\mathcal{L}(d|\eta, \psi) = \mathcal{N}(\eta_0, \sigma_\eta) \mathcal{N}(\psi_0, \sigma_\psi). \quad (\text{A4})$$

Importantly, in this model it is possible for the likelihood to extend to the unphysical regime  $\eta > 0.25$  and  $|\chi_{\text{eff}}| > 1$ , and it is the priors that restrict  $\eta$  and  $\chi_{\text{eff}}$  to their physical ranges. The top panel of Fig. 8 illustrates three example likelihoods selected to mimic the recovered posteriors for our injected signals. Next, we derive the resulting posterior probability densities after changing parameters from  $\theta^a = (\eta, \psi)$  to  $\theta^{a'} = (\eta, \chi_{\text{eff}})$ . Recall that the likelihood of the data given a GW model and set of extrinsic parameters is the same whether we label those extrinsic parameters with  $\theta^{a'}$  or  $\theta^a$ . Thus the likelihood simply transforms as  $\mathcal{L}(d|q, \chi) = \mathcal{L}(d|\eta(q), \psi(q, \chi_{\text{eff}}))$ .

Meanwhile, the posterior probability is proportional to the product of the likelihood and the prior probabilities on the extrinsic parameters  $p(\theta^a)$ . These priors transform according to the Jacobian of  $\partial\theta^{a'}/\partial\theta^a$ , but we can simply

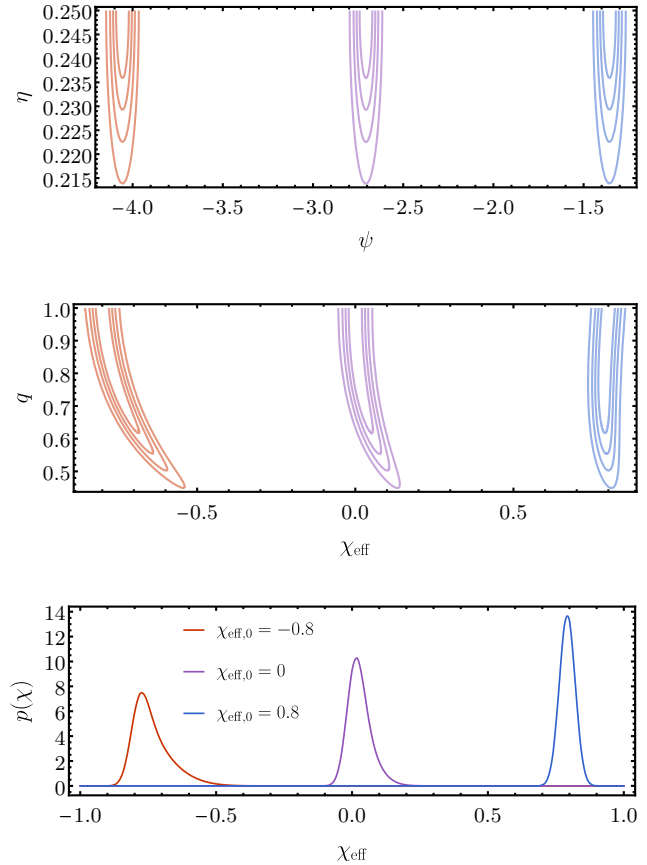


**Figure 8.** Model for the skewness of  $\chi_{\text{eff}}$  posteriors, using Gaussian likelihoods for  $\eta$  and  $\psi$  and flat priors in  $q$  and  $\chi_{\text{eff}}$ . The likelihoods are centered on  $(\eta_0, \chi_{\text{eff},0}) = (0.25, -0.8)$  (red),  $(\eta_0, \chi_{\text{eff},0}) = (0.25, 0)$  (purple) and  $(\eta_0, \chi_{\text{eff},0}) = (0.25, 0.8)$ , (blue), with  $\sigma_\eta = 0.02$  and  $\sigma_\psi = 0.05$ . *Top*: Equally spaced contours of constant likelihood in  $(\eta, \psi)$  coordinates. *Middle*: Equally spaced contours of constant posterior probability in  $(q, \chi_{\text{eff}})$  coordinates, using flat priors in  $q$  and  $\chi_{\text{eff}}$ . *Bottom*: Marginalized  $\chi_{\text{eff}}$  posteriors, displaying positive skew and shifted maxima.

state the priors in terms of  $q$  and  $\chi_{\text{eff}}$  directly. To keep our analysis simple, we select flat priors in  $0 \leq q \leq 1$  and  $-1 \leq \chi_{\text{eff}} \leq 1$ , so that in these ranges our model for the posterior is

$$p(\theta^{a'}|d) \propto p(q, \chi_{\text{eff}}) \mathcal{L}(d|q, \chi_{\text{eff}}) \propto \mathcal{L}(d|q, \chi_{\text{eff}}). \quad (\text{A5})$$

We plot the three posteriors in  $(q, \chi_{\text{eff}})$  in the middle panel of Fig. 8 for the same three likelihoods illustrated in the top panel. The resulting posteriors takes on the characteristic “banana” shape seen in the posteriors recovered from our simulated signals.

Finally we can consider the marginalized posteriors in  $\chi_{\text{eff}}$  in this model. We find that these posteriors have positive skew, as seen in Fig. 8. It is clear from the likelihoods how the tilted posteriors and boundary of  $\eta$  generate skewed posteriors once projected onto  $\chi_{\text{eff}}$ , and

why the effect is greater for likelihoods peaked at more negative  $\chi_{\text{eff}}$ . In addition, the maximum of the posterior is shifted rightward relative to the maximum likelihood in all cases.

We note that while previous studies have discussed how the combination (Cutler & Flanagan 1994; Poisson & Will 1995)

$$\beta = \frac{113 - 76\eta}{12}\chi_{\text{eff}} + \frac{76\delta\eta}{12}\chi_{\alpha} \quad (\text{A6})$$

is better measured than  $\chi_{\text{eff}}$  during the inspiral, reduces degeneracies (see e.g. Pürrer et al. 2013), here we find that it is  $\psi$  that is well measured and weakly correlated with  $\eta$ . We also find that it is the mapping between  $(\eta, \psi)$  and  $(q, \chi_{\text{eff}})$  which reproduces the observed degeneracy.

### B. A RECIPE FOR GENERATING SIMULATED $\chi_{\text{eff}}$ POSTERIOR

In this section we provide a simple recipe for generating simulated posterior distributions for  $\chi_{\text{eff}}$  which go beyond the simple Gaussian approximation, and include the effects we have described in Sec. 3.

We find that posterior distributions for  $\chi_{\text{eff}}$  can be parametrized well with a generalized normal distribution (GND) of type II (Hosking & Wallis 1997).

The probability density function (PDF) of GND of random variable  $x$  can be parameterized by a scale  $\alpha$ , a location  $\xi$  and a shape  $\kappa$ , as

$$p(x) = \frac{\phi(y)}{\alpha - \kappa(x - \xi)}, \quad (\text{B7})$$

where  $\phi(y)$  is the PDF of the standard normal distribution for a random variable  $y$ , defined as

$$y(x; \alpha, \xi, \kappa) = \begin{cases} -\frac{1}{\kappa} \log \left[ 1 - \frac{\kappa(x - \xi)}{\alpha} \right] & \text{if } \kappa \neq 0 \\ \frac{x - \xi}{\alpha} & \text{if } \kappa = 0 \end{cases} \quad (\text{B8})$$

To generate a synthetic posterior distribution for  $\chi_{\text{eff}}$ , we can relate the median  $\tilde{x}$ , standard deviation  $\sigma$  and skewness  $\gamma$  of the  $\chi_{\text{eff}}$  posterior to GND-parameters as follows:

$$\tilde{x} = \xi, \quad (\text{B9})$$

$$\sigma^2 = \frac{\alpha^2}{\kappa^2} e^{\kappa^2} (e^{\kappa^2} - 1), \quad (\text{B10})$$

$$\gamma = \frac{3e^{\kappa^2} - e^{3\kappa^2} - 2}{(e^{\kappa^2} - 1)^{3/2}} \text{sign}(\kappa). \quad (\text{B11})$$

These can be inverted to obtain the  $\alpha$ ,  $\xi$  and  $\kappa$  necessary to simulate the posterior.

A recipe for producing synthetic  $\chi_{\text{eff}}$  posteriors is thus:

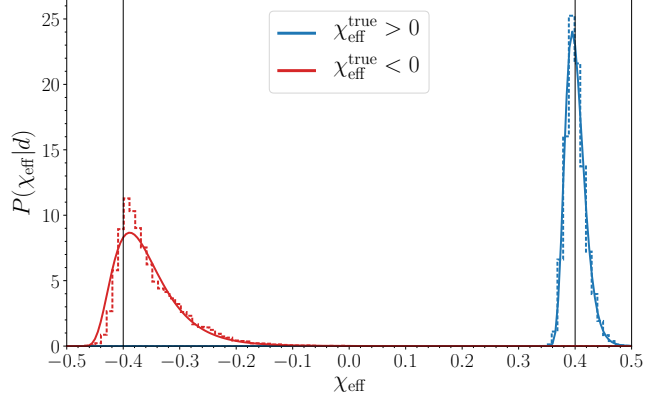


**Figure 9.** Posterior distribution for  $\chi_{\text{eff}}$  for two example BBH sources (histograms) together with the synthetic posteriors produced using the method described in Sec. B. The only difference between the two sources is the sign of  $\chi_{\text{eff}}$ , given in the legend.

- Step 1 – Generate a value for the median from the desired astrophysical distribution. This can be assumed to be the same as the true value, or can be offset from it using the values in Appendix D
- Step 2 – Solve Equation (B11) numerically for  $\kappa$ . The relevant  $\gamma$  can be read from Fig. 3.
- Step 3 – Solve Equation B10 for  $\alpha$ . This equation depends on both  $\sigma$  and  $\kappa$ . The  $\sigma$  of each true  $\chi_{\text{eff}}$  obtained from our MCMC runs are given in Appendix D.
- Step 4 – Use  $\xi$ ,  $\alpha$  and  $\kappa$  so determined with Eqs. B7 and B8 to get  $p(\chi_{\text{eff}})$ .

An illustrative example is shown in Fig. 9 for two posteriors (histograms) and the corresponding synthetic version obtained with the method described above (lines).

In order to make use of these posteriors with alternative prior assumptions, the next step is to divide out the prior probability distribution for  $\chi_{\text{eff}}$  used in our injection and recovery. The prior on  $\chi_{\text{eff}}$  is nontrivial, and combines the priors on the components of the spins  $\chi_i \cdot \hat{\mathbf{L}}$ , and on the component masses. The former assumes that the spins are isotropic in direction and that their dimensionless magnitudes are uniform between zero and 0.89, a restriction chosen as the limit where the accelerated, reduced-order-quadrature likelihood we use is validated over (Smith et al. 2016). The prior on the aligned spin components has the simple analytic form given an upper magnitude  $\chi_*$ ,

$$p(\chi_i \cdot \hat{\mathbf{L}}) = \frac{\ln(|\chi_* / \chi|)}{2\chi_*}. \quad (\text{B12})$$

Meanwhile, the mass priors are uniform in the  $m_1$ - $m_2$  plane but constrained to lie within a range of constant  $\mathcal{M}$  and with additional bounds on the maximum mass and minimum mass ratio (Smith et al. 2016).

We find that we can fit the normalized prior distribution for  $\chi_{\text{eff}}$  with an analytic ansatz dependent on a single width parameter  $w$ . The model is based on the double-exponential distribution, further constrained to require that  $\chi_{\text{eff}}$  fall smoothly to zero at the maximum possible value  $\chi_*$ , which is a property inherited from the prior on  $\chi_i \cdot \hat{\mathbf{L}}$ . Our functional form is

$$p(\chi_{\text{eff}}) = \frac{1 - e^{-(|\chi_{\text{eff}}| - \chi_*)/w}}{2\chi_* + 2w(1 - e^{\chi_*/w})}. \quad (\text{B13})$$

Fitting to each prior individually yields a mean value  $w = 0.23$  with a root-mean-square deviation  $\sigma_w = 0.005$ . We find that  $w = 0.23$  gives an adequate fit to all the  $\chi_{\text{eff}}$  priors used in this study.

A webpage where the readers can generate synthetic  $\chi_{\text{eff}}$  posterior distributions (or likelihood) for the masses, spins and SNR used in this paper can be found at [superstring.mit.edu/welcome.html](http://superstring.mit.edu/welcome.html)

### C. OFFSETS FROM REDUCED ORDER QUADRATURES

As mentioned in the main body, we have used a reduced order quadrature (ROQ) approximation to the likelihood (Smith et al. 2016) implemented within the stochastic parameter estimation code LALINFERENCE. By expressing the overlap between the gravitational wave data and the model waveform using a reduced basis, a ROQ likelihood can achieve speedup factors between  $\sim 10 - 300$  of a generic parameter estimation analysis. The basis applicable for low mass analyses (e.g. neutron star binaries) has recently been found to suffer from an issue (LIGO-Virgo Parameter estimation working group 2017) which, for some combination of masses, spins and SNRs, results in biased posteriors for the chirp mass and other intrinsic parameters, including  $\chi_{\text{eff}}$ . No appreciable bias is observed in the extrinsic parameters (e.g. distance). Thus, the original posteriors we obtained for  $\chi_{\text{eff}}$  for the BNS runs were biased away from their true value.

To correct for this bias we re-analyzed the BNS systems for which  $\chi_{\text{eff}} = 0$  (all three mass ratios) using the same waveform family as before, but without enabling the ROQ likelihood. Not using the ROQ likelihood causes the analysis to become significantly more computationally expensive, which is why we only ran the sources with  $\chi_{\text{eff}} = 0$ , taking them to be representative for all BNS spins. The re-analysis gave posteriors that, while not perfectly centered at the true value, were significantly

closer to it. We have thus calculated the shift between the  $\chi_{\text{eff}}$  median of the ROQ and the non-ROQ runs, and applied those shifts to all the BNS runs, obtaining the points shown in Fig. 5.

We note that BBH systems analyzed with the ROQ method are *not* observed to be affected by this issue. This implies that none of the results published by the LIGO and Virgo collaborations suffer from this issue, since the ROQ method was not used to measure mass and spins of GW170817 (Abbott et al. 2017d).

### D. USEFUL TABLES

In this section we report key statistics for the posterior distributions of  $\chi_{\text{eff}}$  obtained with the simulations described in Sec. 3.

$m_1 - m_2 [M_\odot]$ \backslash $\chi_{\text{eff}}$	-0.7	-0.6	-0.5	-0.4	-0.3	-0.2	-0.1	0	0.1	0.2	0.3	0.4	0.5	0.6	0.7
30-30	0.351	0.344	0.334	0.319	0.307	0.286	0.247	0.227	0.226	0.216	0.203	0.183	0.172	0.159	0.149
30-15	0.471	0.506	0.499	0.484	0.423	0.355	0.294	0.237	0.218	0.195	0.175	0.156	0.135	0.111	0.097
30-10	0.627	0.617	0.588	0.549	0.510	0.449	0.408	0.378	0.322	0.292	0.275	0.241	0.191	0.135	0.088
15-15	0.659	0.613	0.533	0.447	0.375	0.286	0.232	0.179	0.171	0.150	0.136	0.122	0.104	0.092	0.074
15-7.5	0.603	0.633	0.568	0.587	0.525	0.442	0.354	0.278	0.241	0.215	0.185	0.165	0.146	0.107	0.073
15-5	0.562	0.534	0.576	0.542	0.540	0.516	0.539	0.412	0.333	0.289	0.235	0.232	0.182	0.146	0.089
5-5	0.548	0.522	0.499	0.427	0.362	0.292	0.238	0.191	0.181	0.161	0.164	0.138	0.122	0.100	0.062

**Table 2.** 90% credible intervals for BBHs at network SNR of 15. The BHs' tilt angles at 20 Hz are  $10^\circ$ .

$m_1 - m_2 [M_\odot]$ \backslash $\chi_{\text{eff}}$	-0.7	-0.6	-0.5	-0.4	-0.3	-0.2	-0.1	0	0.1	0.2	0.3	0.4	0.5	0.6	0.7
30-30	0.205	0.189	0.183	0.171	0.165	0.153	0.143	0.121	0.122	0.112	0.104	0.093	0.088	0.083	0.078
30-15	0.219	0.231	0.222	0.240	0.222	0.212	0.192	0.146	0.141	0.121	0.106	0.088	0.071	0.056	0.050
30-10	0.257	0.276	0.305	0.326	0.325	0.282	0.210	0.182	0.187	0.185	0.160	0.128	0.088	0.064	0.045
15-15	0.253	0.226	0.200	0.180	0.180	0.168	0.127	0.093	0.090	0.079	0.066	0.059	0.049	0.043	0.038
15-7.5	0.367	0.466	0.506	0.518	0.441	0.353	0.272	0.210	0.169	0.140	0.131	0.120	0.093	0.064	0.043
15-5	0.520	0.467	0.512	0.543	0.461	0.397	0.407	0.334	0.313	0.266	0.211	0.212	0.163	0.122	0.067
5-5	0.263	0.265	0.277	0.238	0.231	0.208	0.167	0.141	0.131	0.113	0.103	0.089	0.081	0.074	0.048

**Table 3.** 90% credible intervals for BBHs at network SNR of 30. The BHs' tilt angles at 20 Hz are  $10^\circ$ .

$m_1 - m_2 [M_\odot]$ \backslash $\chi_{\text{eff}}$	-0.7	-0.6	-0.5	-0.4	-0.3	-0.2	-0.1	0	0.1	0.2	0.3	0.4	0.5	0.6	0.7
30-30	0.346	0.343	0.328	0.318	0.304	0.282	0.247	0.228	0.225	0.220	0.199	0.189	0.169	0.160	0.148
30-15	0.407	0.441	0.477	0.467	0.428	0.365	0.292	0.239	0.216	0.194	0.171	0.153	0.135	0.111	0.096
30-10	0.524	0.567	0.557	0.545	0.500	0.479	0.413	0.381	0.324	0.287	0.271	0.239	0.183	0.122	0.081
15-15	0.676	0.598	0.533	0.447	0.360	0.283	0.210	0.185	0.163	0.156	0.133	0.118	0.104	0.089	0.075
15-7.5	0.604	0.654	0.643	0.573	0.517	0.446	0.350	0.284	0.227	0.221	0.191	0.164	0.143	0.105	0.071
15-5	0.491	0.576	0.566	0.528	0.468	0.516	0.525	0.427	0.344	0.289	0.249	0.235	0.178	0.140	0.081
5-5	0.578	0.537	0.485	0.425	0.354	0.294	0.220	0.208	0.190	0.180	0.166	0.146	0.131	0.100	0.062

**Table 4.** 90% credible intervals for BBHs at network SNR of 15. The BHs' tilt angles at 20 Hz are  $30^\circ$ .

$m_1 - m_2 [M_\odot]$ \backslash $\chi_{\text{eff}}$	-0.7	-0.6	-0.5	-0.4	-0.3	-0.2	-0.1	0	0.1	0.2	0.3	0.4	0.5	0.6	0.7
30-30	0.204	0.195	0.184	0.168	0.162	0.152	0.141	0.120	0.119	0.114	0.102	0.095	0.088	0.085	0.078
30-15	0.220	0.219	0.219	0.232	0.235	0.216	0.186	0.147	0.138	0.124	0.101	0.087	0.072	0.055	0.049
30-10	0.324	0.292	0.298	0.321	0.333	0.287	0.227	0.176	0.186	0.176	0.168	0.125	0.081	0.055	0.043
15-15	0.230	0.201	0.193	0.183	0.183	0.164	0.121	0.097	0.085	0.076	0.066	0.057	0.051	0.043	0.038
15-7.5	0.390	0.452	0.505	0.483	0.412	0.338	0.260	0.214	0.183	0.158	0.132	0.115	0.094	0.063	0.041
15-5	0.346	0.391	0.459	0.473	0.425	0.371	0.374	0.357	0.310	0.260	0.243	0.203	0.157	0.111	0.055
5-5	0.246	0.262	0.267	0.244	0.238	0.209	0.170	0.136	0.125	0.102	0.099	0.092	0.085	0.071	0.044

**Table 5.** 90% credible intervals for BBHs at network SNR of 30. The BHs' tilt angles at 20 Hz are  $30^\circ$ .

$m_1 - m_2 [M_\odot]$ \backslash $\chi_{\text{eff}}$	-0.2	-0.15	-0.1	-0.05	0	0.05	0.1	0.15	0.2
1.4-1.4	0.237	0.204	0.184	0.152	0.138	0.136	0.126	0.120	0.110
2.0-1.4	0.272	0.241	0.214	0.185	0.167	0.153	0.139	0.142	0.129
2.2-1.3	0.309	0.270	0.239	0.204	0.184	0.167	0.152	0.139	0.135

**Table 6.** 90% credible intervals for BNSs at network SNR of 15. The spins are aligned with the orbital angular momentum.

$m_1 - m_2 [M_\odot]$ \(\chi_{\text{eff}}\)	-0.2	-0.15	-0.1	-0.05	0	0.05	0.1	0.15	0.2
1.4-1.4	0.089	0.088	0.081	0.072	0.059	0.056	0.054	0.053	0.051
2.0-1.4	0.122	0.115	0.110	0.097	0.081	0.076	0.073	0.068	0.066
2.2-1.3	0.148	0.144	0.130	0.118	0.097	0.082	0.077	0.072	0.072

**Table 7.** 90% credible intervals for BNSs at network SNR of 30. The spins are aligned with the orbital angular momentum.

$m_1 - m_2 [M_\odot]$ \(\chi_{\text{eff}}\)	-0.7	-0.6	-0.5	-0.4	-0.3	-0.2	-0.1	0	0.1	0.2	0.3	0.4	0.5	0.6	0.7
30-30	0.106	0.104	0.102	0.098	0.094	0.087	0.075	0.068	0.069	0.066	0.062	0.056	0.053	0.048	0.045
30-15	0.140	0.150	0.149	0.147	0.131	0.111	0.092	0.072	0.067	0.059	0.053	0.047	0.041	0.034	0.029
30-10	0.199	0.199	0.189	0.177	0.160	0.136	0.121	0.113	0.097	0.091	0.086	0.076	0.060	0.041	0.027
15-15	0.216	0.204	0.181	0.147	0.123	0.093	0.072	0.057	0.054	0.047	0.043	0.038	0.032	0.028	0.023
15-7.5	0.195	0.207	0.178	0.181	0.163	0.141	0.114	0.090	0.077	0.069	0.058	0.052	0.045	0.032	0.022
15-5	0.180	0.166	0.180	0.166	0.161	0.154	0.161	0.132	0.105	0.093	0.076	0.073	0.057	0.046	0.027
5-5	0.163	0.162	0.165	0.142	0.120	0.096	0.077	0.064	0.058	0.054	0.053	0.044	0.038	0.031	0.019

**Table 8.** Standard deviation for BBHs at network SNR of 15. The BHs' tilt angles at 20 Hz are  $10^\circ$ .

$m_1 - m_2 [M_\odot]$ \(\chi_{\text{eff}}\)	-0.7	-0.6	-0.5	-0.4	-0.3	-0.2	-0.1	0	0.1	0.2	0.3	0.4	0.5	0.6	0.7
30-30	0.062	0.058	0.056	0.052	0.049	0.047	0.044	0.037	0.037	0.034	0.032	0.029	0.027	0.025	0.024
30-15	0.067	0.069	0.067	0.072	0.067	0.063	0.059	0.044	0.043	0.037	0.032	0.027	0.022	0.017	0.015
30-10	0.078	0.083	0.094	0.099	0.098	0.086	0.065	0.055	0.057	0.057	0.049	0.039	0.027	0.020	0.014
15-15	0.081	0.073	0.065	0.058	0.057	0.052	0.040	0.030	0.028	0.025	0.021	0.018	0.015	0.013	0.011
15-7.5	0.116	0.140	0.156	0.158	0.135	0.112	0.090	0.067	0.055	0.046	0.041	0.038	0.030	0.020	0.013
15-5	0.152	0.145	0.159	0.168	0.145	0.120	0.117	0.095	0.095	0.087	0.069	0.068	0.054	0.039	0.021
5-5	0.089	0.080	0.088	0.078	0.074	0.071	0.055	0.044	0.043	0.037	0.034	0.030	0.027	0.023	0.015

**Table 9.** Standard deviation for BBHs at network SNR of 30. The BHs' tilt angles at 20 Hz are  $10^\circ$ .

$m_1 - m_2 [M_\odot]$ \(\chi_{\text{eff}}\)	-0.7	-0.6	-0.5	-0.4	-0.3	-0.2	-0.1	0	0.1	0.2	0.3	0.4	0.5	0.6	0.7
30-30	0.105	0.104	0.100	0.097	0.092	0.086	0.075	0.069	0.069	0.067	0.061	0.058	0.051	0.048	0.045
30-15	0.124	0.132	0.145	0.144	0.132	0.114	0.091	0.072	0.067	0.059	0.052	0.047	0.041	0.034	0.029
30-10	0.162	0.176	0.177	0.173	0.155	0.145	0.124	0.111	0.098	0.090	0.084	0.076	0.057	0.037	0.025
15-15	0.222	0.199	0.178	0.148	0.118	0.090	0.067	0.058	0.052	0.049	0.042	0.036	0.032	0.027	0.023
15-7.5	0.195	0.213	0.200	0.174	0.156	0.143	0.114	0.091	0.075	0.069	0.060	0.052	0.044	0.032	0.022
15-5	0.151	0.177	0.181	0.161	0.142	0.154	0.159	0.136	0.110	0.092	0.080	0.073	0.057	0.044	0.025
5-5	0.168	0.167	0.153	0.146	0.116	0.095	0.073	0.067	0.062	0.059	0.053	0.045	0.040	0.031	0.019

**Table 10.** Standard deviation for BBHs at network SNR of 15. The BHs' tilt angles at 20 Hz are  $30^\circ$ .

$m_1 - m_2 [M_\odot]$ \(\chi_{\text{eff}}\)	-0.7	-0.6	-0.5	-0.4	-0.3	-0.2	-0.1	0	0.1	0.2	0.3	0.4	0.5	0.6	0.7
30-30	0.061	0.060	0.056	0.051	0.049	0.046	0.042	0.036	0.036	0.035	0.031	0.029	0.027	0.026	0.024
30-15	0.067	0.065	0.066	0.070	0.071	0.065	0.056	0.044	0.042	0.038	0.030	0.026	0.022	0.017	0.015
30-10	0.099	0.088	0.090	0.098	0.101	0.087	0.069	0.054	0.057	0.053	0.051	0.038	0.025	0.017	0.013
15-15	0.075	0.064	0.061	0.060	0.057	0.051	0.039	0.030	0.027	0.024	0.020	0.017	0.016	0.013	0.011
15-7.5	0.116	0.135	0.157	0.149	0.129	0.107	0.085	0.068	0.059	0.051	0.042	0.036	0.030	0.019	0.012
15-5	0.106	0.118	0.141	0.148	0.136	0.112	0.111	0.102	0.089	0.084	0.077	0.064	0.049	0.033	0.017
5-5	0.080	0.083	0.088	0.079	0.077	0.070	0.056	0.044	0.040	0.035	0.033	0.030	0.027	0.022	0.014

**Table 11.** Standard deviation for BBHs at network SNR of 30. The BHs' tilt angles at 20 Hz are  $30^\circ$ .

$m_1 - m_2 [M_\odot]$ \(\backslash\) \(\chi_{\text{eff}}\)	-0.2	-0.15	-0.1	-0.05	0	0.05	0.1	0.15	0.2
1.4-1.4	0.078	0.067	0.060	0.051	0.046	0.044	0.040	0.039	0.036
2.0-1.4	0.091	0.081	0.072	0.061	0.054	0.050	0.047	0.047	0.042
2.2-1.3	0.103	0.090	0.079	0.068	0.060	0.054	0.051	0.046	0.045

**Table 12.** Standard deviation for BNSs at network SNR of 15. The spins are aligned with the orbital angular momentum.

$m_1 - m_2 [M_\odot]$ \(\backslash\) \(\chi_{\text{eff}}\)	-0.2	-0.15	-0.1	-0.05	0	0.05	0.1	0.15	0.2
1.4-1.4	0.030	0.029	0.026	0.024	0.020	0.019	0.018	0.018	0.017
2.0-1.4	0.041	0.038	0.036	0.032	0.027	0.025	0.024	0.022	0.022
2.2-1.3	0.050	0.046	0.042	0.038	0.033	0.027	0.025	0.024	0.023

**Table 13.** Standard deviation for BNSs at network SNR of 30. The spins are aligned with the orbital angular momentum.

$m_1 - m_2 [M_\odot]$ \(\backslash\) \(\chi_{\text{eff}}\)	-0.7	-0.6	-0.5	-0.4	-0.3	-0.2	-0.1	0	0.1	0.2	0.3	0.4	0.5	0.6	0.7
30-30	0.100	0.119	0.065	0.085	-0.052	-0.120	-0.213	0.004	0.077	-0.073	-0.150	-0.120	-0.110	-0.065	-0.085
30-15	0.745	0.658	0.524	0.378	0.219	0.021	0.128	0.285	0.583	0.400	0.357	0.318	0.043	-0.109	-0.072
30-10	0.159	0.069	-0.150	-0.581	-0.633	-0.750	-0.605	-0.197	0.265	0.572	0.562	0.391	0.143	-0.179	-0.179
15-15	0.209	0.246	0.372	0.318	0.618	0.751	1.007	1.556	1.403	1.363	1.232	1.011	0.693	0.330	-0.004
15-7.5	-0.738	-0.777	-0.721	-0.595	-0.329	0.027	0.402	1.161	1.549	1.744	1.579	1.478	1.138	0.692	0.261
15-5	-1.008	-1.201	-0.996	-1.153	-1.178	-0.762	-0.382	0.091	0.593	1.630	1.556	1.353	1.110	0.770	0.366
5-5	0.538	0.200	0.254	0.408	0.443	0.710	1.204	1.712	1.757	1.818	1.712	1.530	1.297	0.710	0.353

**Table 14.** Skewness for BBHs at network SNR of 15. The BHs' tilt angles at 20 Hz are  $10^\circ$ .

$m_1 - m_2 [M_\odot]$ \(\backslash\) \(\chi_{\text{eff}}\)	-0.7	-0.6	-0.5	-0.4	-0.3	-0.2	-0.1	0	0.1	0.2	0.3	0.4	0.5	0.6	0.7
30-30	-0.021	-0.002	-0.146	-0.087	-0.082	-0.032	-0.143	0.001	-0.120	-0.050	-0.076	-0.101	-0.047	-0.008	-0.057
30-15	-0.047	-0.092	0.046	0.050	0.106	-0.006	-0.104	-0.105	0.134	0.073	0.009	0.089	-0.014	-0.062	0.004
30-10	0.148	0.260	0.140	0.065	-0.037	-0.414	-0.534	-0.524	0.034	-0.269	-0.272	-0.440	-0.342	-0.138	0.061
15-15	0.535	0.968	1.098	1.471	1.444	1.165	0.838	1.276	1.125	1.046	0.964	0.773	0.509	0.139	0.019
15-7.5	1.132	0.668	0.531	0.310	-0.030	-0.069	0.268	0.560	1.105	1.091	1.223	1.026	0.926	0.695	0.455
15-5	0.153	0.543	0.288	-0.318	-0.831	-0.735	-0.871	-0.534	0.082	0.768	0.901	0.831	0.459	0.331	0.351
5-5	0.696	0.623	0.814	1.142	1.077	0.888	1.121	1.628	1.305	1.463	1.600	1.818	1.548	1.049	1.076

**Table 15.** Skewness for BBHs at network SNR of 30. The BHs' tilt angles at 20 Hz are  $10^\circ$ .

$m_1 - m_2 [M_\odot]$ \(\backslash\) \(\chi_{\text{eff}}\)	-0.7	-0.6	-0.5	-0.4	-0.3	-0.2	-0.1	0	0.1	0.2	0.3	0.4	0.5	0.6	0.7
30-30	0.052	0.071	0.092	0.037	0.036	-0.139	-0.233	0.001	0.062	-0.122	-0.138	-0.129	-0.098	-0.077	-0.133
30-15	0.609	0.611	0.517	0.363	0.157	0.155	0.094	0.338	0.548	0.463	0.350	0.235	0.047	-0.104	-0.046
30-10	-0.133	0.057	-0.166	-0.393	-0.672	-0.774	-0.570	-0.249	0.251	0.629	0.628	0.481	-0.002	-0.135	-0.194
15-15	0.175	0.067	0.272	0.519	0.518	0.809	0.990	1.419	1.491	1.302	1.171	0.947	0.576	0.248	0.061
15-7.5	-0.371	-0.633	-0.671	-0.655	-0.400	0.105	0.541	1.242	1.652	1.502	1.492	1.414	1.184	0.749	0.231
15-5	-0.027	-0.190	-0.547	-1.015	-1.027	-0.710	-0.242	0.159	0.759	1.464	1.531	1.361	1.032	0.574	0.223
5-5	0.571	0.447	0.189	0.324	0.379	0.633	1.125	1.586	1.556	1.932	1.672	1.609	1.144	0.770	0.374

**Table 16.** Skewness for BBHs at network SNR of 15. The BHs' tilt angles at 20 Hz are  $30^\circ$ .

$m_1 - m_2 [M_\odot]$ \(\backslash\) \(\chi_{\text{eff}}\)	-0.7	-0.6	-0.5	-0.4	-0.3	-0.2	-0.1	0	0.1	0.2	0.3	0.4	0.5	0.6	0.7
30-30	0.056	-0.115	-0.091	0.003	-0.008	-0.135	-0.077	-0.128	-0.060	-0.068	-0.072	-0.067	-0.049	-0.039	-0.076
30-15	-0.152	-0.130	0.231	0.159	0.045	-0.008	-0.160	-0.055	0.137	0.032	0.057	-0.010	0.006	0.029	0.029
30-10	0.320	0.009	0.017	0.032	-0.115	-0.373	-0.505	-0.289	-0.001	-0.319	-0.435	-0.361	-0.171	-0.020	0.080
15-15	1.128	1.128	1.266	1.375	1.426	1.168	0.934	1.265	1.128	1.004	1.033	0.776	0.393	0.185	-0.079
15-7.5	0.929	0.758	0.481	0.271	0.074	-0.050	0.050	0.630	1.057	1.193	1.194	1.161	0.676	0.588	0.321
15-5	0.193	0.054	0.134	-0.000	-0.582	-0.874	-0.814	-0.431	0.145	0.668	0.608	0.246	0.355	0.109	0.128
5-5	1.036	0.662	0.783	1.052	1.139	0.658	0.899	1.663	1.501	1.814	2.006	1.819	1.611	1.435	1.150

**Table 17.** Skewness for BBHs at network SNR of 30. The BHs' tilt angles at 20 Hz are  $30^\circ$ .

$m_1 - m_2 [M_\odot]$ \(\backslash\) \(\chi_{\text{eff}}\)	-0.2	-0.15	-0.1	-0.05	0	0.05	0.1	0.15	0.2
1.4-1.4	0.962	1.031	1.059	1.413	1.668	1.605	1.769	1.777	1.748
2.0-1.4	0.787	0.911	1.107	1.250	1.540	1.705	1.684	1.889	1.831
2.2-1.3	0.593	0.720	0.895	1.201	1.279	1.621	1.711	1.739	1.759

**Table 18.** Skewness for BNSs at network SNR of 15. The spins are aligned with the orbital angular momentum.

$m_1 - m_2 [M_\odot]$ \(\backslash\) \(\chi_{\text{eff}}\)	-0.2	-0.15	-0.1	-0.05	0	0.05	0.1	0.15	0.2
1.4-1.4	1.996	1.837	1.798	1.814	1.961	2.181	1.938	2.065	2.040
2.0-1.4	1.840	1.626	1.538	1.518	1.667	2.069	2.035	1.965	1.934
2.2-1.3	1.803	1.474	1.417	1.330	1.424	1.830	1.902	1.951	1.708

**Table 19.** Skewness for BNSs at network SNR of 30. The spins are aligned with the orbital angular momentum.

$m_1 - m_2 [M_\odot]$ \(\backslash\) \(\chi_{\text{eff}}\)	-0.7	-0.6	-0.5	-0.4	-0.3	-0.2	-0.1	0	0.1	0.2	0.3	0.4	0.5	0.6	0.7
30-30	-0.486	-0.430	-0.367	-0.292	-0.216	-0.131	-0.049	0.017	0.097	0.195	0.290	0.382	0.474	0.565	0.657
30-15	-0.510	-0.462	-0.391	-0.324	-0.235	-0.150	-0.085	-0.015	0.059	0.161	0.266	0.367	0.475	0.578	0.680
30-10	-0.384	-0.336	-0.268	-0.164	-0.131	-0.082	-0.054	-0.024	0.010	0.076	0.190	0.311	0.439	0.562	0.674
15-15	-0.352	-0.329	-0.305	-0.214	-0.195	-0.123	-0.046	0.024	0.117	0.215	0.309	0.406	0.503	0.598	0.693
15-7.5	-0.112	-0.112	-0.086	-0.093	-0.094	-0.096	-0.067	-0.035	0.038	0.140	0.246	0.352	0.465	0.578	0.685
15-5	-0.167	-0.089	-0.083	-0.055	-0.046	-0.062	-0.049	-0.057	-0.027	0.020	0.138	0.262	0.391	0.525	0.658
5-5	-0.443	-0.321	-0.280	-0.237	-0.170	-0.103	-0.050	0.028	0.120	0.216	0.313	0.411	0.511	0.616	0.711

**Table 20.** Median of  $\chi_{\text{eff}}$  for BBHs at network SNR of 15. The BHs' tilt angles at 20 Hz are  $10^\circ$ .

$m_1 - m_2 [M_\odot]$ \(\backslash\) \(\chi_{\text{eff}}\)	-0.7	-0.6	-0.5	-0.4	-0.3	-0.2	-0.1	0	0.1	0.2	0.3	0.4	0.5	0.6	0.7
30-30	-0.629	-0.549	-0.459	-0.373	-0.279	-0.182	-0.083	0.004	0.098	0.195	0.294	0.392	0.489	0.585	0.683
30-15	-0.618	-0.556	-0.476	-0.392	-0.293	-0.192	-0.095	-0.006	0.073	0.180	0.281	0.380	0.484	0.584	0.688
30-10	-0.608	-0.550	-0.471	-0.376	-0.260	-0.149	-0.064	-0.001	0.066	0.168	0.272	0.382	0.484	0.581	0.682
15-15	-0.595	-0.540	-0.449	-0.368	-0.273	-0.172	-0.073	0.013	0.109	0.206	0.302	0.399	0.497	0.596	0.694
15-7.5	-0.492	-0.488	-0.383	-0.323	-0.199	-0.140	-0.095	-0.023	0.040	0.144	0.249	0.354	0.464	0.575	0.684
15-5	-0.438	-0.458	-0.373	-0.225	-0.113	-0.099	-0.053	-0.014	0.013	0.062	0.161	0.289	0.421	0.549	0.667
5-5	-0.613	-0.480	-0.417	-0.351	-0.242	-0.156	-0.066	0.017	0.119	0.213	0.311	0.404	0.506	0.607	0.704

**Table 21.** Median of  $\chi_{\text{eff}}$  for BBHs at network SNR of 30. The BHs' tilt angles at 20 Hz are  $10^\circ$ .

$m_1 - m_2 [M_\odot]$ \(\backslash\) \(\chi_{\text{eff}}\)	-0.7	-0.6	-0.5	-0.4	-0.3	-0.2	-0.1	0	0.1	0.2	0.3	0.4	0.5	0.6	0.7
30-30	-0.470	-0.419	-0.366	-0.293	-0.219	-0.133	-0.050	0.019	0.095	0.193	0.290	0.385	0.478	0.567	0.655
30-15	-0.487	-0.451	-0.389	-0.307	-0.230	-0.155	-0.080	-0.017	0.054	0.158	0.266	0.370	0.475	0.580	0.686
30-10	-0.276	-0.316	-0.262	-0.199	-0.126	-0.081	-0.055	-0.024	0.010	0.074	0.185	0.304	0.453	0.575	0.685
15-15	-0.358	-0.281	-0.270	-0.252	-0.186	-0.125	-0.047	0.026	0.118	0.215	0.310	0.407	0.505	0.600	0.693
15-7.5	-0.185	-0.128	-0.092	-0.076	-0.083	-0.088	-0.078	-0.034	0.037	0.141	0.249	0.357	0.468	0.583	0.692
15-5	-0.366	-0.297	-0.155	-0.066	-0.042	-0.053	-0.077	-0.052	-0.028	0.025	0.140	0.270	0.400	0.542	0.675
5-5	-0.463	-0.377	-0.264	-0.236	-0.155	-0.095	-0.040	0.028	0.125	0.219	0.315	0.410	0.516	0.616	0.711

**Table 22.** Median of  $\chi_{\text{eff}}$  for BBHs at network SNR of 15. The BHs' tilt angles at 20 Hz are  $30^\circ$ .

$m_1 - m_2 [M_\odot]$ \(\backslash\) \(\chi_{\text{eff}}\)	-0.7	-0.6	-0.5	-0.4	-0.3	-0.2	-0.1	0	0.1	0.2	0.3	0.4	0.5	0.6	0.7
30-30	-0.611	-0.537	-0.454	-0.371	-0.282	-0.184	-0.086	0.004	0.098	0.196	0.296	0.395	0.491	0.589	0.684
30-15	-0.573	-0.526	-0.467	-0.389	-0.294	-0.191	-0.090	-0.006	0.079	0.183	0.282	0.384	0.484	0.587	0.695
30-10	-0.493	-0.464	-0.419	-0.365	-0.260	-0.146	-0.063	-0.005	0.070	0.166	0.274	0.382	0.485	0.587	0.690
15-15	-0.644	-0.546	-0.454	-0.368	-0.271	-0.172	-0.075	0.014	0.109	0.206	0.302	0.401	0.500	0.597	0.697
15-7.5	-0.520	-0.475	-0.359	-0.284	-0.208	-0.137	-0.078	-0.029	0.043	0.144	0.253	0.358	0.474	0.584	0.691
15-5	-0.498	-0.451	-0.383	-0.267	-0.118	-0.091	-0.058	-0.020	0.018	0.058	0.197	0.332	0.437	0.570	0.684
5-5	-0.638	-0.496	-0.421	-0.340	-0.255	-0.138	-0.054	0.017	0.117	0.212	0.306	0.404	0.505	0.607	0.706

**Table 23.** Median of  $\chi_{\text{eff}}$  for BBHs at network SNR of 30. The BHs' tilt angles at 20 Hz are  $30^\circ$ .

$m_1 - m_2 [M_\odot]$ \(\backslash\) \(\chi_{\text{eff}}\)	-0.2	-0.15	-0.1	-0.05	0	0.05	0.1	0.15	0.2
1.4-1.4	-0.144	-0.101	-0.057	-0.016	0.024	0.071	0.118	0.167	0.216
2.0-1.4	-0.147	-0.109	-0.070	-0.026	0.014	0.056	0.105	0.155	0.203
2.2-1.3	-0.144	-0.113	-0.076	-0.039	0.006	0.045	0.093	0.142	0.194

**Table 24.** Median of  $\chi_{\text{eff}}$  for BNSs at network SNR of 15. The spins are aligned with the orbital angular momentum.

$m_1 - m_2 [M_\odot]$ \(\backslash\) \(\chi_{\text{eff}}\)	-0.2	-0.15	-0.1	-0.05	0	0.05	0.1	0.15	0.2
1.4-1.4	-0.187	-0.135	-0.086	-0.037	0.012	0.060	0.109	0.158	0.207
2.0-1.4	-0.205	-0.153	-0.102	-0.051	-0.003	0.044	0.094	0.145	0.195
2.2-1.3	-0.221	-0.168	-0.117	-0.068	-0.016	0.030	0.082	0.133	0.183

**Table 25.** Median of  $\chi_{\text{eff}}$  for BNSs at network SNR of 30. The spins are aligned with the orbital angular momentum.

## REFERENCES

- Aasi, J., et al. 2015, *CQG*, 32, 074001
- Abadie, J., et al. 2010, *CQG*, 27, 173001
- Abbott, B. P., et al. 2016a, *PRX*, 6, 041015
- . 2016b, *PRL*, 116, 241103
- . 2016c, *PRL*, 116, 061102
- . 2016d, *LRR*, 19, 1
- . 2016e, *ApJ*, 833, L1
- . 2016f, *ApJ*, 832, L21
- . 2017a, *PRL*, 118, 221101
- . 2017b, *ApJ*, 851, L35
- . 2017c, *PRL*, 119, 141101
- . 2017d, *PRL*, 119, 161101
- Acernese, F., Agathos, M., Agatsuma, K., et al. 2015, *CQG*, 32, 024001
- Ajith, P., Hannam, M., Husa, S., et al. 2011, *PRL*, 106, 241101
- Baird, E., Fairhurst, S., Hannam, M., & Murphy, P. 2013, *PRD*, 87, 024035
- Belczynski, K., Taam, R. E., Rantsiou, E., & van der Sluys, M. 2008, *ApJ*, 682, 474
- Benacquista, M. J., & Downing, J. M. B. 2013, *LRR*, 16, 4
- Blanchet, L. 2014, *LRR*, 17, 2
- Breivik, K., Rodriguez, C. L., Larson, S. L., Kalogera, V., & Rasio, F. A. 2016, *ApJ*, 830, L18
- Campanelli, M., Lousto, C. O., & Zlochower, Y. 2006, *PRD*, 74, 041501
- Chatziioannou, K., Cornish, N., Klein, A., & Yunes, N. 2014, *PRD*, 89, 104023
- . 2015, *ApJ*, 798, L17
- Chatziioannou, K., Lovelace, G., Boyle, M., et al. 2018, *ArXiv e-prints*, arXiv:1804.03704
- Corsaro, E., Lee, Y.-N., García, R. A., et al. 2017, *Nature Astronomy*, 1, 0064
- Cutler, C., & Flanagan, É. E. 1994, *PRD*, 49, 2658
- Damour, T. 2001, *PRD*, 64, 124013
- Farr, B., Holz, D. E., & Farr, W. M. 2018, *ApJ*, 854, L9
- Farr, W. M., Stevenson, S., Miller, M. C., et al. 2017, *Nature*, 548, 426
- Gerosa, D., Kesden, M., Berti, E., O’Shaughnessy, R., & Sperhake, U. 2013, *PRD*, 87, 104028
- Gerosa, D., Kesden, M., Sperhake, U., Berti, E., & O’Shaughnessy, R. 2015, *PRD*, 92, 064016
- Gerosa, D., O’Shaughnessy, R., Kesden, M., Berti, E., & Sperhake, U. 2014, *PRD*, 89, 124025
- Hannam, M., Schmidt, P., Bohé, A., et al. 2014, *PRL*, 113, 151101
- Hosking, J. R. M., & Wallis, J. R. 1997, *Regional Frequency Analysis: An Approach Based on L-Moments* (Cambridge University Press), doi:10.1017/CBO9780511529443
- Kalogera, V. 2000, *ApJ*, 541, 319
- Kesden, M., Gerosa, D., O’Shaughnessy, R., Berti, E., & Sperhake, U. 2015, *PRL*, 114, 081103
- Kidder, L. E., Will, C. M., & Wiseman, A. G. 1993, *PRD*, 47, R4183
- LIGO-Virgo Parameter estimation working group. 2017, *Private Communication*
- Mandel, I., & O’Shaughnessy, R. 2010, *Classical and Quantum Gravity*, 27, 114007
- Miller, M. C., & Lauburg, V. M. 2009, *ApJ*, 692, 917
- Nishizawa, A., Berti, E., Klein, A., & Sesana, A. 2016, *PRD*, 94, 064020
- Nishizawa, A., Sesana, A., Berti, E., & Klein, A. 2017, *MNRAS*, 465, 4375
- Poisson, E., & Will, C. M. 1995, *PRD*, 52, 848
- Postnov, K. A., & Yungelson, L. R. 2014, *LRR*, 17, 3
- Pürrer, M., Hannam, M., Ajith, P., & Husa, S. 2013, *PRD*, 88, 064007
- Racine, É. 2008, *PRD*, 78, 044021
- Rodriguez, C. L., Farr, B., Raymond, V., et al. 2014, *ApJ*, 784, 119
- Rodriguez, C. L., Zevin, M., Pankow, C., Kalogera, V., & Rasio, F. A. 2016, *ApJ*, 832, L2
- Santamaría, L., Ohme, F., Ajith, P., et al. 2010, *PRD*, 82, 064016
- Scheel, M. A., Giesler, M., Hemberger, D. A., et al. 2015, *CQG*, 32, 105009
- Schmidt, P., Ohme, F., & Hannam, M. 2015, *PRD*, 91, 024043
- Smith, R., Field, S. E., Blackburn, K., et al. 2016, *PRD*, 94, 044031
- Stevenson, S., Berry, C. P. L., & Mandel, I. 2017, *MNRAS*, 471, 2801
- Talbot, C., & Thrane, E. 2017, *PRD*, 96, 023012
- Vallisneri, M. 2008, *PRD*, 77, 042001
- Veitch, J., Raymond, V., Farr, B., et al. 2015, *PRD*, 91, 042003
- Vitale, S., Gerosa, D., Haster, C.-J., Chatziioannou, K., & Zimmerman, A. 2017a, *PRL*, 119, 251103
- Vitale, S., Lynch, R., Raymond, V., et al. 2017b, *PRD*, 95, 064053
- Vitale, S., Lynch, R., Sturani, R., & Graff, P. 2017c, *CQG*, 34, 03LT01
- Wiseman, A. G. 1992, *PRD*, 46, 1517
- Wysocki, D., Gerosa, D., O’Shaughnessy, R., et al. 2018a, *PRD*, 97, 043014
- Wysocki, D., Lange, J., & O’Shaughnessy, R. 2018b, *In preparation*

Zhu, X.-J., Thrane, E., Osłowski, S., Levin, Y., & Lasky,  
P. D. 2017, ArXiv e-prints, arXiv:1711.09226